Design and Analysis of a New Hybrid Wireless Power Transfer System With a Space-Saving Coupler Structure

Xingran Gao, Chunhua Liu, *Senior Member, IEEE*, Hong Zhou, *Member, IEEE*, Wenshan Hu, *Member, IEEE*, Yongcan Huang, *Student Member, IEEE*, Yang Xiao, *Student Member, IEEE*, Zhongcheng Lei, *Member, IEEE*, and Jing Chen

***Abstract*—This article is to present the design, analysis, and verification of a new hybrid wireless power transfer (HWPT) system, which has a space-saving coupler structure. The key of the design is to simplify the two coupling capacitor plates into one single frame-shaped plate at each side. Then, the coupling coil for inductive power transfer (IPT) is embedded into the metal frame to form a compact hybrid coupler. Meanwhile, the coupling polarity between the coils is specified to realize the superposition of the inductive and capacitive coupling. As a result, the proposed HWPT system can offer a good comprise of efficiency promotion and a space-saving coupler structure simultaneously. To illustrate the system working principles, the equivalent circuit model is first derived. Then, a detailed analysis is conducted in terms of the reflected impedance. Consequently, the mechanism of the efficiency promotion can be clearly explained. Finally, a prototype is constructed with several experiments, which validate the effectiveness of the proposed HWPT system. Results show that an efficiency increase of 14% over the pure IPT is obtained at 35-cm distance. Moreover, the effects of varying the resonant frequency are also carried out to instruct the practical system design.**

***Index Terms*—Capacitive power transfer (CPT), hybrid coupler, hybrid power transfer, resonant frequency, wireless power transfer (WPT).**

Manuscript received May 24, 2020; revised August 10, 2020; accepted September 18, 2020. Date of publication September 28, 2020; date of current version January 22, 2021. The work was supported in part by a grant from Shenzhen–Hong Kong Innovation Circle Category D Project from the Science Technology and Innovation Committee of Shenzhen Municipality, China, under Project SGDX2019081623101559, in part by a grant from ITF Platform of Innovation and Technology Commission of Hong Kong SAR under Project ITP/027/19AP, in part by Strategic Research Grant under Projects CityU11218519 and CityU11217520, and in part by Applied Research Grant from the City University of Hong Kong, Hong Kong, under Project 9667214. Recommended for publication by Associate Editor A. Safaee. *(Corresponding authors: Chunhua Liu; Wenshan Hu.)*

Xingran Gao, Chunhua Liu, Yongcan Huang, and Yang Xiao are with the School of Energy and Environment, City University of Hong Kong, Hong Kong (e-mail: gaoxran@foxmail.com; chunliu@cityu.edu.hk; ansel.shaw@my.cityu.edu.hk; yongcan.huang@my.cityu.edu.hk).

Hong Zhou, Wenshan Hu, Zhongcheng Lei, and Jing Chen are with the School of Electrical Engineering and Automation, Wuhan University, Wuhan 430072, China (e-mail: hzhouwuhee@whu.edu.cn; wenshan.hu@whu.edu.cn; zhongcheng.lei@whu.edu.cn; drchen@whu.edu.cn).

Color versions of one or more of the figures in this article are available online at https://ieeexplore.ieee.org.

Digital Object Identifier 10.1109/TPEL.2020.3027473

I. Introduction

In recent years, wireless power transfer (WPT) technologies have been extensively used in various applications, such as for charging electric vehicles (EVs) [1], [2], power transmission line monitoring (PTLM) devices [3], [4], and so on. In general, inductive power transfer (IPT) and capacitive power transfer (CPT) are the two most pervasive methods to realize WPT [5]. For IPT, it uses the magnetic field to deliver the power wirelessly. For CPT, it employs the electric field to form the power transfer channel. Currently, the IPT has been widely studied for industrial and domestic scenarios, where the power level ranges from several watts to tens of kilo watts [6]–[9]. The CPT is also attracting more and more attention in recent years, as it is more penetrative for metal barriers with the thinner, lighter, and less costly couplers [11]–[14].

Actually, for both the IPT and CPT with a resonant structure, the inductive and capacitive reactance exists simultaneously and compensates each other. Essentially, when the resonance occurs, a high frequency magnetic field and electric field will be generated concurrently across the resonant inductor. Thus, it is possible to combine both the inductive coupling and the capacitive coupling to form a hybrid wireless power transfer (HWPT) system [15]–[19]. As a result, such a hybrid system is likely to have a stronger coupling ability, i.e., a larger reflected impedance than the pure IPT system.

Prominently, the stronger coupling ability of the HWPT can bring many advantages for WPT applications. For instance, for EV charging applications, the coupling coil can be made smaller since the extra capacitive coupling will compensate the reduced inductive coupling. Consequently, the whole system will be lighter, less costly, and more resistive to foreign metal objects. For the PTLM applications with large transfer gaps [3], [4], the power transfer efficiency (PTE) can be improved with the same coil sizes. As a result, the power supply for outdoor monitoring devices will be more robust. As investigated in [15], the combination of the inductive and CPT will open a wide choice for power management between the IPT and the CPT.

Several works have been investigated on the working principles and performance of the HWPT system. First, a HWPT structure with integrated coupling plates was proposed in [16]. Its topology is shown in Fig. 1(a). On one hand, the two plates

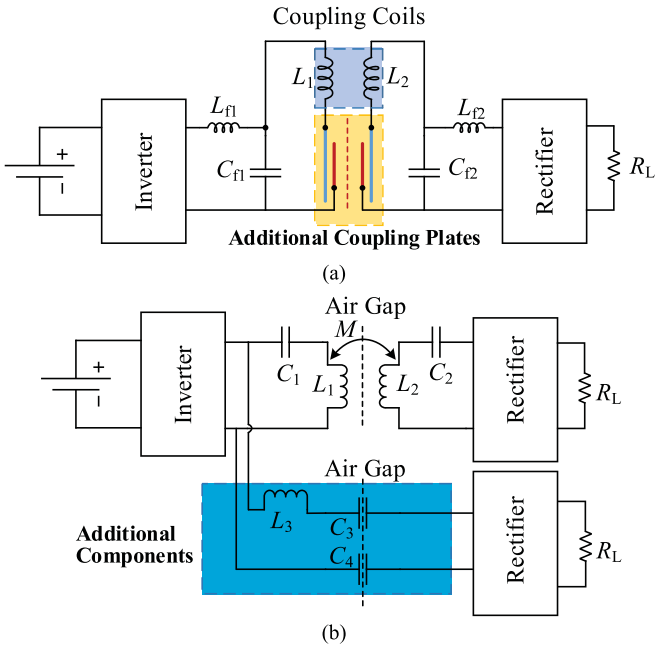

Fig. 1. Previous hybrid WPT structures. (a) Hybrid structure using common inductors and coupling plates. (b) Hybrid structure with an external resonator.

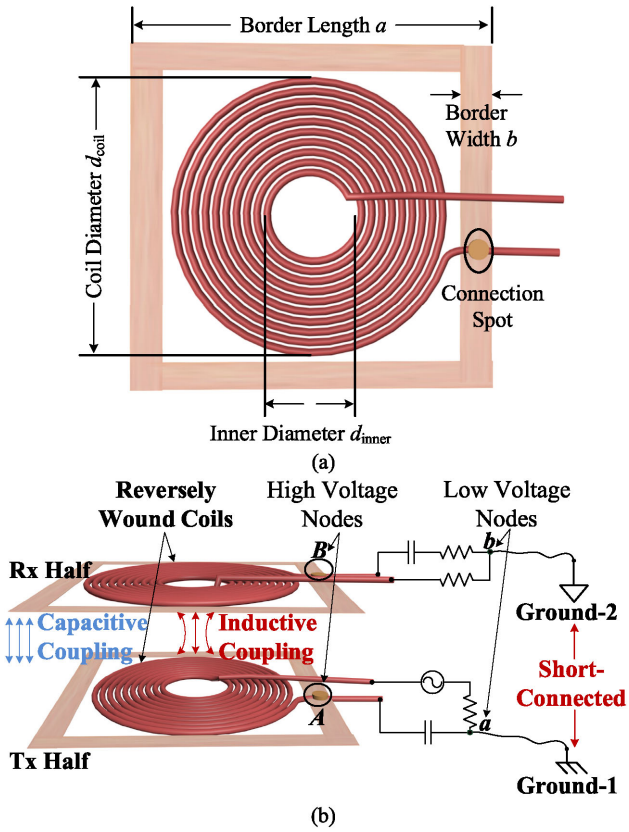

Fig. 2. Proposed hybrid coupler structure. (a) Single half exhibition. (b) Overall system structure.

on the one side formed the resonant capacitor. On the other hand, they also formed the coupling capacitor with the plates on the other side. However, due to the separated placement of the coil and the plates, extra area of one plate was needed at each side. Then, in [17], the inductive and capacitive couplers were further integrated into a single coupler. The way is to fold the plates of aluminum sheets to increase its self-inductance. However, the folded aluminum sheets formed a relatively large volume. Besides, in [18], a general model was proposed for a hybrid system, where various resonant topologies could be chosen to resonate the system. Unfortunately, extra areas of two plates were needed at each side. Furthermore, in [19], a hybrid system for railway application was presented with an analysis of its antimisalignment performance. The coupling plates were placed above or below the coils to save the couplers' horizontal size. Regrettably, the couplers' vertical height was increased. Additionally, in [20] and [21], a hybrid structure with an extra resonant loop was presented. As shown in Fig. 1(b), an external inductor with two coupling capacitors was added, which forms an additional single series-resonant loop. However, strictly speaking, the systems in [20] and [21] were not an inductive and capacitive combined hybrid system. This is because the IPT branch and the CPT branch were compensated separately from each other.

According to the above review, one major drawback of the existing HWPT systems is the increased coupler sizes due to the two extra coupling plates at each side. The increased size, in either horizontal or vertical direction, may result in more difficulties for practical installation. Moreover, in [16]–[19], the hybrid system is analyzed in terms of the superposed output power. Regrettably, the analysis in terms of efficiency contribution is still absent for the HWPT. In addition, the resonant frequencies in these literatures are fixed at one certain value. Nevertheless, the optimal resonant frequency (ORF) for the HWPT may change with the transfer gap varying. Thus, the ORF for the HWPT at various transfer gaps should be explored to instruct the practical system design.

In this article, a new HWPT system is proposed, which is capable to provide a good comprise of efficiency promotion and a compact coupler structure. Fig. 2 shows the system structure, where an inner coil and outer frame coupler structure is adopted to form the inductive and capacitive combined coupling. Actually, the key is to establish an effective capacitive coupling loop with only one pair of frame-shaped metal frames. First, the design procedure of proposed HWPT system is introduced. Then, the system performance is analyzed in terms of the reflected impedance to clarify the function of each coupling. After that, the resonant frequency is optimized for various transfer gaps. As a result, the transmitter can adapt to receivers with different sizes and transfer gaps. Finally, experiments are carried out to verify the effectiveness of proposed HWPT system. Additionally, a detailed comparison with the previous designs is given in Table III in the Appendix.

II. Design Procedure of the Proposed Hybrid WPT System

The proposed hybrid coupler is shown in Fig. 2(a), where the coupling coil is embedded inside a metal frame. The inner coil is

used to establish both the inductive coupling and the resonance with the lumped compensated capacitor. The outer thin metal frame is connected to the high voltage resonant node of the coil. Then, the two parallel frames form a supplementary capacitive route to further promote the coupling. Essentially, the proposed hybrid coupler can fully use both the magnetic field and the electric field. Thus, by using this coupler structure, the proposed HWPT system is more likely to achieve a good balance between a high PTE and lightweight with low cost.

The system design procedure includes three steps. First, the plates for the capacitive coupling should be reduced from two to one at each side. Second, a proper frame-shaped coupling plate needs to be designed to achieve both a compact structure and one comparable coupling capacitance. Finally, a suitable circuit structure should be established so that the effects of the inductive coupling and the capacitive coupling can interfere constructively instead of destructively.

A. Reducing Coupling Plates

Reducing the number of the coupling plates is based on a survey of suitable WPT scenarios. Essentially, these scenarios have a common feature that the reference grounds of the Tx and Rx sides can be directly or equivalently short-connected, as shown in Fig. 2(b). Thus, only one coupling capacitor is needed to form the capacitive coupling loop. The suitable scenarios include but are not limited to the following.

1) *For railway EVs:* As seen in [12] and [19], the chassis of the railway vehicle is connected to the track and the ground through its metal wheels. As a result, the wheels, the track, and the ground can be performed as a circuit return path. Thus, the low voltage nodes *a* and *b* in Fig. 2(b) can be considered as short-connected and one coupling capacitor can be removed.
2) *For roadway EVs:* As seen in [22], the vehicle body can be directly connected to the ground shield through metallic brushes. Thus, only one coupling capacitor is needed.
3) *For PTLM applications:* On one hand, due to the need of shielding, the reference ground of the Tx side is connected to the power transmission line, and the Rx side can be grounded [3], [4]. On the other hand, calculation results show that the capacitance between the overhead line and the ground can exceed 6 nF per kilo meters [23]. This capacitance is far larger than the coupling capacitance in CPT systems, which is commonly several or tens of picofarad. Thus, in such cases, nodes *a* and *b* in Fig. 2(b) are equivalently short-connected.
4) *For EVs with large metal chassis:* As seen in [24], a two-plate CPT system can still work effectively, if the stray capacitance between the chassis and the ground is used as the current return route. This stray capacitance was tested as 82 pF, which was several times of the 15-pF coupling capacitance. Consequently, the total equivalent coupling capacitance, i.e., the series equivalent values of 82 and 15 pF, is 12.7 pF. Thus, in such cases, the chassis and the ground can be seemed as short-circuited but with a slightly smaller coupling capacitance.

TABLE I
COIL DIMENSIONS

Symbol	Parameter	Value
d_{coil}	Coil Outer Diameter	20 cm
d_{inner}	Coil Inner Diameter	3 cm
N_t	Turn Number	35
d_{bundle}	Wire Bundle Diameter	2.1 mm
d_{strand}	Wire Strand Diameter	0.04 mm
N_{strand}	Strand Number	1200
s_{turn}	Turn Spacing	0.3 mm
a_{plate}	Outer Border Length of The Plates	24 cm
b_{frame}	Border Width of The Frames	2 cm
t_{plate}	Thickness of The Plates	1 mm

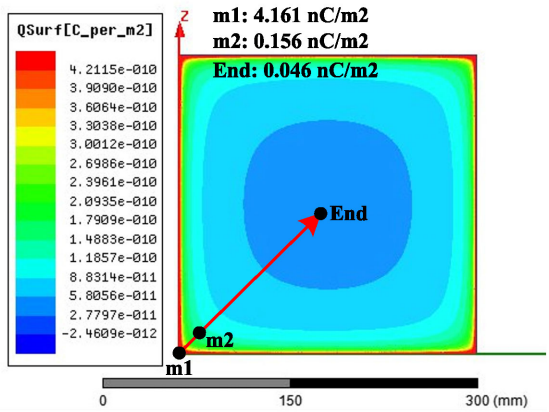

Fig. 3. Charge density on the full-area coupling plate.

5) *For special WPT applications:* As stated in [25], each passive conductor has a self-capacitance or stray capacitance with respect to the ground. If the conductor is large enough, an effective return route can be built with the self-capacitance or the stray capacitance or the combination of them. However, considering the lack of specific application scenarios, such cases will not be further studied in this article.

Generally, for scenarios 1) through 5), the coupling plates at the low voltage side can be eliminated, and the two plates at the resonant high voltage nodes are reserved.

B. Shaping Metal Frames

The fringe effect of charge distribution is used to shape the coupling metal frames. The fringe effect means that charges are concentrated at the edges of the coupling plates, when the gap is relatively large [26], [27]. As a result, the edges contribute more to the coupling capacitance than the inner area.

First, the charge distribution on a full-area plate is simulated with the finite-element analysis (FEA) software. The plate parameters used for the simulation are listed in Table I. Then, Fig. 3 gives the charge distribution on the full-area square plate when a pair of the plates is coupled at 35-cm distance. As seen in Fig. 3, the charge density at location "m1" is 26 times of that at location "m2." Thus, most of the inner area can be removed while maintaining one comparable coupling capacitance simultaneously.

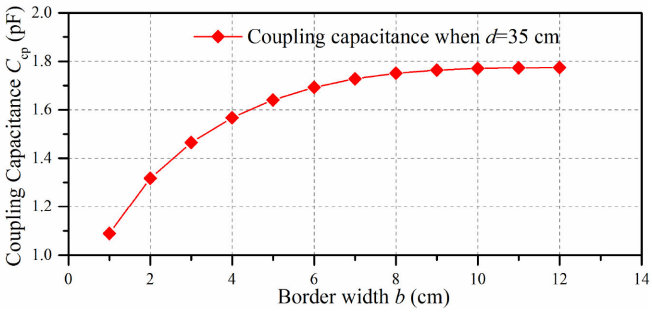

Fig. 4. Simulated coupling capacitance C_{cp} versus various border width b.

Second, to obtain a proper border width, the relationship between the coupling capacitance C_{cp} and the border width b is studied. The simulated C_{cp}-b curve is shown in Fig. 4. When the border width is 2 cm, the C_{cp} has a value of 1.32 pF. It is approximately 75% of the coupling capacitance of the full-area coupling plates. This result indicates that even if 70% of the plate area is removed, 75% of the total coupling capacitance can still be maintained. Thus, the metal frame is designed with a 2-cm width since this width provides a good balance between a compact frame structure and one comparable coupling capacitance. Then, the coupling coil is embedded inside the metal frame to form the hybrid coupler.

It is noted that coils of various types can be embedded, including the square solenoid coils, the circular solenoid coils, and the planar spiral coils. Due to the virtues of small thickness, the planar spiral coil is used as an example in this article.

C. Designing Circuit Structure

First, the series–series resonant topology is selected for the sake of convenient analysis of the system's basic characteristics. As shown in Fig. 2(b), a lumped capacitor is used as the compensation capacitor. Using a lumped compensation capacitor can bring at least two advantages over the parallel-plate compensation capacitor in [16] and [19]. First of all, the compensation capacitance will be less sensitive to the surroundings. Moreover, the extra space of the plates is no longer needed.

Second, special attention should be paid to the coupling polarity of the Tx and Rx coils [16]. As seen in Fig. 2(b), the Tx coil is wound in counterclockwise direction, while the Rx coil is wound in the clockwise direction. Under such configurations, the effects of the inductive coupling and the capacitive coupling can be superposed. Conversely, if the two coils are wound in the same direction, the effects of the two coupling would cancel each other out. The performance with different coupling polarities will be compared in Sections III and IV.

So, the key features of the proposed HWPT system are summarized as follows.

1) The proposed HWPT system adopts only one coupling capacitor to construct the capacitive coupling loop, which makes the system structure much simpler.
2) The full-area coupling plate at each side is simplified into a frame-shaped plate. Thus, the coil and the plate can be integrated as one compact hybrid coupler.

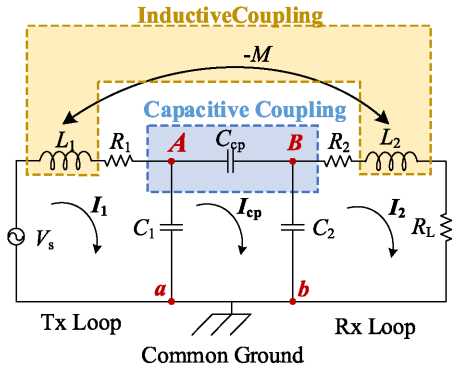

Fig. 5. Equivalent circuit of the proposed HWPT system.

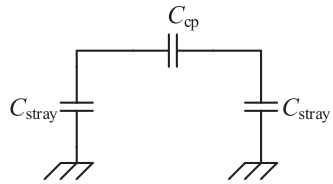

Fig. 6. Capacitance structure of a mid-range parallel frame capacitor.

3) The Tx and Rx coils are wound with different directions to superpose the effects of both the inductive coupling and the capacitive coupling.

III. Analysis of System Performance

A. Circuit Model

First, the equivalent circuit of Fig. 2(b) is derived as Fig. 5, which contains three loops. In Fig. 5, C_1 and C_2 represent the total compensation capacitance of the Tx resonator and the Rx resonator, respectively. C_{cp} is the coupling capacitance between the two frame-shaped plates. L_1 and L_2 are the inductances of the Tx and Rx coils, respectively, and their parasitic resistances are labeled as R_1 and R_2, respectively. The ac driving source is denoted as V_s, and the load is represented by R_L. The mutual inductance between the two coils is represented by $-M$ since the two coils are reversely wound. Besides, the working current in the three loops is denoted by I_1, I_{cp}, and I_2 in turn.

It is noted that C_1 and C_2 comprise two parts: the capacitance of the series-connected lumped compensation capacitor and the stray capacitances of the metal frames. As shown in Fig. 6, two parallel plates have three capacitances: one coupling capacitance C_{cp} and two stray capacitances C_{stray}. C_{cp} is formed by the electric coupling between the two plates, while C_{stray} is formed by the stray coupling of each plate to the ground and surroundings. However, for the sake of convenient analysis, the two stray capacitances are absorbed in C_1 and C_2, respectively, and only C_{cp} are shown in Fig. 5.

Then, the working current in each loop can be derived using Kirchhoff's voltage law. For simplicity, the impedances of the

three loops are predefined as follows:

$$\begin{cases} Z_1 = R_1 + j\omega L_1 + \frac{1}{j\omega C_1} \\ Z_{\text{coup}} = Z_{C1} + Z_{Ccp} + Z_{C2} \\ Z_2 = R_L + R_2 + j\omega L_2 + \frac{1}{j\omega C_2} \end{cases} \tag{1}$$

where Z_{C1}, Z_{coup}, and Z_{C2} are the reactance of C_1, C_{cp}, and C_2, respectively.

And then, the model in Fig. 5 can be expressed as

$$\begin{pmatrix} Z_1 - Z_{C1} & j\omega M \\ -Z_{C1} & Z_{\text{coup}} - Z_{C2} \\ j\omega M & -Z_{C2} \quad Z_2 \end{pmatrix} \begin{pmatrix} I_1 \\ I_{cp} \\ I_2 \end{pmatrix} = \begin{pmatrix} V_s \\ 0 \\ 0 \end{pmatrix}. \tag{2}$$

Consequently, the working current in the Tx and Rx loops can be derived as

$$\begin{cases} I_1 = \frac{V_s}{Z_1 + T + 2j\omega MS + \omega^2 M^2 R} \\ I_2 = I_1 (S - j\omega MR) \end{cases} \tag{3}$$

where T, S, and R are expressed as follows:

$$T = -\frac{{Z_{C1}}^2}{Z_{\text{total}}} \tag{4}$$

$$S = \frac{Z_{C1} Z_{C2}}{Z_2 Z_{\text{total}}} \tag{5}$$

$$R = \frac{{Z_{C2}}^2}{Z_{\text{total}} {Z_2}^2} + \frac{1}{Z_2} \tag{6}$$

where Z_{total} represents the total impedance of the second loop with consideration of the reflected impedance from the Rx loop and can be expressed as

$$Z_{\text{total}} = Z_{\text{coup}} - \frac{{Z_{C2}}^2}{Z_2}. \tag{7}$$

Then, using (3), the input power and the output power can be expressed as follows:

$$P_{\text{in}} = V_s \cdot \text{Re}\,(I_1) \tag{8}$$

$$P_{\text{out}} = |I_2|^2 \cdot R_L \tag{9}$$

So, the PTE can be represented by

$$\eta = \frac{P_{\text{out}}}{P_{\text{in}}} = \frac{|I_2|^2 R_L}{V_s \text{Re}\,(I_1)}. \tag{10}$$

Here, V_s, I_1, and I_2 all represent their rms values.

B. Parameter Calculation

To evaluate the system performance under various transfer gaps, the values of the mutual inductance M and the coupling capacitance C_{cp} versus distance d should be derived first.

First, the values of M are measured experimentally with the methods in [28]. Let L_X be the total inductance when the two coils are series connected with a positive mutual inductance. Then, let L_Y be the total inductance when they are connected with a negative mutual inductance. Then, M and the coupling factor k can be expressed as

$$M = k\sqrt{L_1 L_2} = \frac{L_X - L_Y}{4}. \tag{11}$$

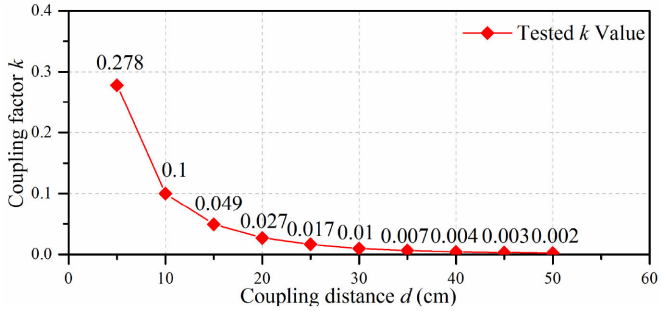

Fig. 7. Tested results of k values.

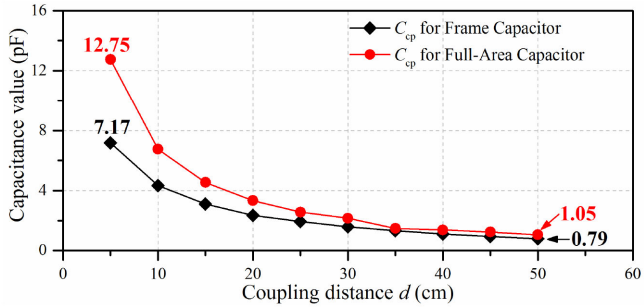

Fig. 8. Simulated values of C_{cp} versus distance d.

For practical coupling coils whose dimensions are listed in Table I, the tested k values are plotted in Fig. 7, which degrade rapidly as d increases. Besides, the tested self-inductance is approximately 125 μH.

Then, based on the results in Fig. 4, metal frames with a 24-cm border length and a 2-cm border width are used to construct the coupling capacitor. For the evaluation of C_{cp}, its values can be obtained by both the 3-D FEA simulation and the experimental testing. However, the experimental testing was slightly affected by the stray coupling, particularly when the transfer gap is large. Thus, the simulation method is employed to evaluate the C_{cp}.

The simulated capacitance values of the frame-shaped capacitor are shown in Fig. 8. For the sake of comparison, the capacitance values of the full-area capacitor are also depicted. As one can see, the frame capacitor has a 7.17-pF coupling capacitance at 5-cm distance, which is 56.24% of that of the full-area capacitor. With d increasing, this ratio increases to a value of 75.24% at the 50-cm distance. At this distance, C_{cp} is 0.79 pF for the frame capacitor and 1.05 pF for the full-area capacitor. This is because with d increasing, charges are more concentrated to the edges. Consequently, the elimination of the inner area has a lower influence on the coupling capacitance. Furthermore, with a comparison between Figs. 7 and 8, one can see that C_{cp} declines much slower than k. This result implies that the HWPT system may exhibit more significant advantages over the pure IPT system at a larger transfer gap.

C. System Performance

First, the circuit parameters are tested from the practical prototype. The results are listed in Table II. Among them, L_1,

TABLE II
CIRCUIT PARAMETERS

Parameter	Value	Parameter	Value
L_1, L_2	125 μH	C_1, C_2	460 pF
R_1, R_2	1.36 Ω	R_L	23.34 Ω

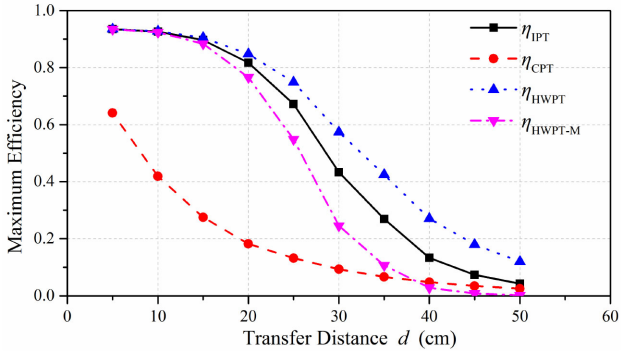

Fig. 9. Comparison of calculated efficiencies.

L_2, C_1, C_2, and R_1, R_2 are all tested using an Agilent E4980AL LCR meter at 640 kHz.

Second, the PTE values at various transfer gaps are calculated. By substituting the tested M in Fig. 7, the simulated $C_{\rm cp}$ in Fig. 8, and the parameters in Table II in (10), the PTE values of the HWPT can be obtained. Let $\eta_{\rm HWPT}$, $\eta_{\rm IPT}$, $\eta_{\rm CPT}$, and $\eta_{\rm HWPT\text{-}M}$ represent the maximum efficiency of the HWPT, the pure IPT, the pure CPT, and the HWPT, but with a positive mutual inductance, respectively. Then, a comparison of their calculated values is shown in Fig. 9.

As seen in Fig. 9, for the proposed HWPT, an evident efficiency promotion over the pure IPT system is achieved when d is larger than 20 cm. For instance, when d is 30 cm, $\eta_{\rm HWPT}$ has a value of 57.42%, which is 14.06% higher than $\eta_{\rm IPT}$ and 48.11% higher than $\eta_{\rm CPT}$. This result indicates that the IPT and the CPT can be effectively combined using the proposed hybrid structure. In contrast, when the winding direction of the Rx coil is reversed, i.e., the two coils have the same winding direction, the PTE will be adversely affected. As a result, the $\eta_{\rm HWPT\text{-}M}$ in Fig. 9 is much lower than the $\eta_{\rm IPT}$.

Third, the mechanism of the efficiency promotion is fundamentally explained with the reflected impedance theory. First, according to (3), the system's overall impedance seen from the inverter is

$$Z_{\rm overall} = Z_1 + T + 2j\omega MS + \omega^2 M^2 R \tag{12}$$

where $(T + 2j\omega MS + \omega^2 M^2 R)$ is the total reflected impedance on the Tx loop and its real part determines the efficiency. Then, the total reflected real part is divided into three parts: the part from capacitive coupling $Z_{\rm real\_cap}$, the part from inductive coupling $Z_{\rm real\_indu}$, and the part from the interactive effect of the two coupling $Z_{\rm real\_inter}$. The three parts are expressed as

$$\begin{cases} Z_{\rm real\_cap} = {\rm Re}\,(T) \\ Z_{\rm real\_indu} = {\rm Re}\left(\omega^2 M^2 R\right) \\ Z_{\rm real\_inter} = {\rm Re}\,(2j\omega MS)\,. \end{cases} \tag{13}$$

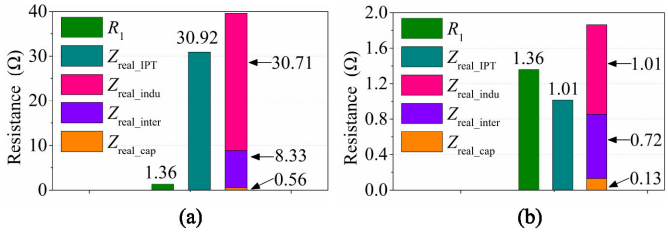

Fig. 10. Comparison of the reflected real part when the system is in resonant state. (a) At 15-cm distance. (b) At 30-cm distance.

Besides, the real part of the pure IPT is expressed as [29]

$$Z_{\rm real\_IPT} = {\rm Re}\left(\omega^2 M^2 / Z_2\right). \tag{14}$$

Then, the comparison of these reflected real parts is shown in Fig. 10, where the system is in resonant state. As one can see, when the distance is 15 cm, the reflected real parts of the HWPT and the pure IPT are both much larger than the Tx resistance R_1. In this case, though the total reflected real part of HWPT is 8.68 Ω larger than the pure IPT, the HWPT does not present an apparent efficiency increase over the IPT. This is because their efficiencies are already at a high level. However, when the distance is 30 cm and the reflected real part is comparable to the Tx resistance, the HWPT exhibits an evident advantage. In Fig. 10(b), the total reflected real part of HWPT is 1.86 Ω, which is nearly two times of $Z_{\rm real\_IPT}$. Here, the contributions of the inductive coupling, the capacitive coupling and their interactive effect are 54.3%, 7%, and 38.7%, respectively. Thus, the promoted coupling is not a simple addition of the pure IPT and the pure CPT. Essentially, their interactive effect also contributes a significant part.

On the other hand, if M has a positive value, the value of $Z_{\rm real\_inter}$ in Fig. 10(b) will be −0.72 Ω. Consequently, the total reflected real part of the HWPT will be reduced to 0.42 Ω. Correspondingly, a lower efficiency than the pure IPT can be observed in Fig. 9.

In general, the proposed HWPT can provide an evident efficiency promotion when the transfer gap is relatively large. In small gap occasions, the increased reflected real part also implies the possibility that the coupling coils can be made smaller while maintaining a close efficiency value.

D. Resonant Frequency Optimization

Practically, one hybrid transmitter may serve receivers with various sizes or transfer gaps, i.e., various values of M and $C_{\rm cp}$. For different occasions, the ORF may also be different. Thus, it will be meaningful to study the effects of varying the resonant frequency $f_{\rm res}$ to instruct the practical system design.

Generally, when transfer gap is relatively small, $f_{\rm res}$ can be lowered to reduce the coil resistance and the loss on power electronics. When transfer gap is relatively large, $f_{\rm res}$ should be promoted to compensate the reduced coupling. For quantified analysis, the η-$f_{\rm res}$ curves should be calculated.

First, the coil's frequency-dependent resistance is tested from 110 kHz to 1 MHz. The tested results are shown in Fig. 11. Then, using (10) and the tested results of M, $C_{\rm cp}$, R_1, and R_2,

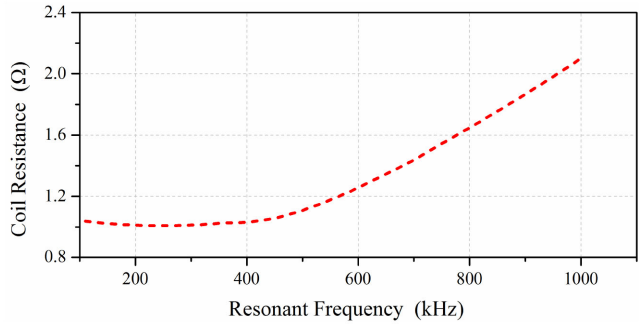

Fig. 11. Coil's frequency-dependent resistance.

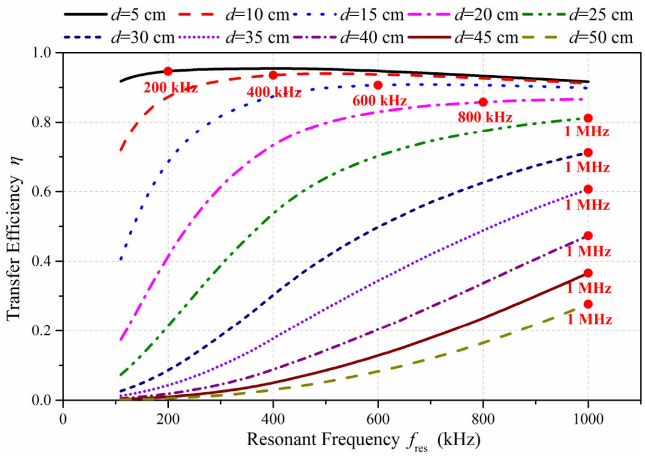

Fig. 12. Efficiency η versus resonant frequency $f_{\rm res}$ at various transfer gaps.

the η-$f_{\rm res}$ curves at various transfer gaps can be obtained, which are depicted in Fig. 12. Besides, the values of the ORF are also marked by the red dots in Fig. 12.

On one hand, when transfer gap is 5 cm, the PTE can reach 95% at only 200 kHz. A further increase of the resonant frequency would result in a higher coil resistance and, consequently, a lower PTE. In the case of 5-cm transfer gap and 200 kHz resonant frequency, the added value of $Z_{\rm real\_cap}$ and $Z_{\rm real\_inter}$ is 0.79 Ω, which contributes only 1% to the total reflected real part. This result indicates that the two coupling frames will benefit little to the PTE when the resonant frequency is relatively low.

On the other hand, when the transfer gap is relatively large, the ORF will be relatively high to compensate the reduced values of both M and $C_{\rm cp}$. For instance, when transfer gap is 30 cm, the ORF for maximum efficiency reaches to 1 MHz. In this case, the added value of $Z_{\rm real\_cap}$ and $Z_{\rm real\_inter}$ is 5.05 Ω and contribute 69.5% to the total reflected real part. This result shows that the two added coupling frames can effectively benefit the PTE when the resonant frequency is relatively high.

So, the effects of varying the resonant frequency can be concluded as follows.

1) The larger the transfer gap is, the higher the resonant frequency should be.
2) The higher the resonant frequency is, the more obvious the contribution by the two extra coupling frames will be.

E. Practical Application Discussion

First, based on the above analysis, a design procedure is summarized to instruct the practical design of the transfer link. Actually, the key is to establish the function relationship among the system performance (namely the transferred power and the PTE), the coupler's dimensions, and the nominal resonant frequency. Then, researchers can choose the proper parameters according to their own priorities. Generally, the design procedure includes seven steps.

1) Constructing a two-plate CPT structure. This is to ensure that the low-voltage resonant nodes of the two sides can be directly or equivalently short-connected.
2) Confirming the ranges of the couplers' dimensions and the nominal resonant frequency. Commonly, the coils have regular shapes, such as the planar spiral, the cylinder solenoid, etc. Whereas, the plates are much more flexible and can be cut into irregular shapes to fit the practical available space.
3) Evaluating the mutual inductance and the coupling capacitance as functions of the coils' and the plates' dimensions. The mutual inductance can be predicted according to [30] and [31], and the coupling capacitance can be calculated with the FEA software.
4) Evaluating the coils' resistances as functions of the nominal resonant frequency and the coil's dimensions. The calculation of coil's high frequency resistance can refer to [32]–[34].
5) Confirming other rated circuit parameters. The needed parameters include the rated driving source voltage and the rated equivalent load resistance.
6) Calculating the transferred power and the PTE according to (3)–(10).
7) Choosing the proper values of the couplers' dimensions and the nominal resonant frequency. For different applications, the priorities may be different. Since the system performance under various couplers' dimensions and resonant frequencies can be predicted with the above steps, researchers can choose the proper configurations according to their own priorities.

Second, some concerns on the system robustness are discussed with suggestions of available solutions. The concerns mainly include three issues.

1) Handling the frequency splitting phenomenon with small transfer gaps. Actually, for the proposed HWPT system, the frequency splitting means that the output power has two peaks against the operating frequency. Whereas, the PTE does not split, and the maximum PTE is always achieved near the nominal resonant frequency, as shown in Fig. 13. Thus, to handle this issue, the key is to improve the output power at the maximum PTE frequency. Three solutions are suggested here. The first one is to decrease the nominal resonant frequency, thus reducing the reflected impedance. The second one is to

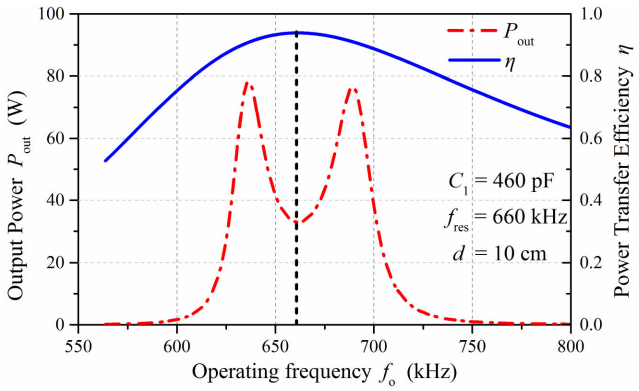

Fig. 13. Frequency splitting phenomenon of the HWPT system.

simply improve the driving source voltage. The third one is to use inductor-capacitor-capacitor (LCC)/inductor-capacitor-inductor (LCL) topology to get rated power at rated transfer gap [16], [17], [35], [36].

2) Handling the sudden receiver-moving-away cases. In this case, a large current will be generated in the series-compensated Tx coil, which may result in device burning down. To tackle this problem, generally two approaches can be employed. One is to sense and control [37]. The other is to implement T-type based compensation topologies, such as the LCC and LCL topologies [35], [36]. As a result, the Tx resonant current can be maintained constant in the sudden receiver-moving-away cases. In addition, a parallel resonant topology at the Tx side can also prevent the overcurrent when the receiver is removed [38].
3) Handling the load resistance variation. Typically, if a battery load is used, its equivalent load resistance will change during the charging process. The load variation may result in efficiency decline when the load deviates from the optimal value. To tackle this problem, one typical way is to use a boost–buck converter to regulate the equivalent load resistance. Thus, the optimal load resistance can be tracked [39].

Third, a T-type based LCC topology is designed as an example, as it is capable to handle the frequency splitting, the distance variation, and the load variation. Usually, the LCC topology is used to realize a constant Tx resonant current and a unit power factor of the inverter's output. As its design procedure has been illustrated in detail in [35] and [36], this article directly gives the design results and performance of the LCC topology. As shown in Fig. 14(a), the designed values of the L_{p1}, C_{p1}, and L_{p2} are 5.8 μH, 10 nF, and 5.8 μH, respectively. Here, the system has a nominal resonant frequency of 660 kHz. Then, as seen in Fig. 14(b), the LCC-compensated HWPT system presents a constant Tx resonant current against the distance and load variations. Moreover, the system's output power automatically increases with the distance decreasing, regardless of the frequency splitting. This is because, when the Tx resonant current keeps constant, the received power is proportional to the reflected impedance.

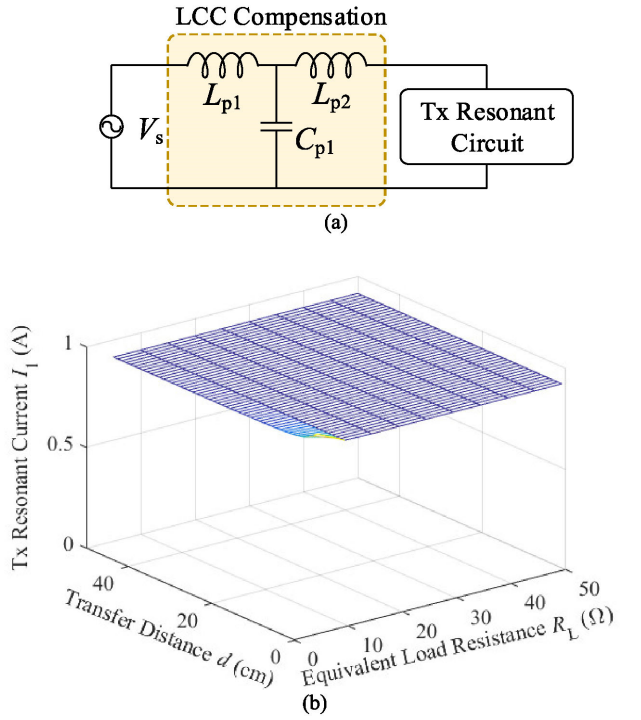

Fig. 14. LCC topology and its effects. (a) LCC circuit structure. (b) Its effects to maintain a constant Tx resonant current.

IV. Practical Experiments

A. Prototype and Experimental Setup

An experimental prototype is constructed to verify the proposed hybrid system, as shown in Fig. 15. A direct digital synthesizer module is adopted to generate accurate square wave exciting signals. The signals are amplified with a gate driver module, and then drive a MOSFET half-bridge to generate an ac voltage from a dc power supply. The Tx loop is energized with the ac and transmits power to the Rx loop through the combined inductive and capacitive coupling. The received ac is rectified into dc using a full-bridge rectifier at the Rx side. The output dc is filtered using capacitors before it drives a resistive load.

As seen in Fig. 15(b), the half-bridge inverter is constructed by GaN-MOSFETs GS66516B from GaN Systems. Moreover, the spiral coils are wound with 1200-strand Litz-wire with a single strand radius of 20 μm. Particularly, the two coils are reversely wound so that the "–M" in Fig. 5 can be established. Besides, high voltage ceramic capacitors are used as the compensation capacitors C_1 and C_2 due to their low resistance and high withstand voltage. A bulb of 24 V/20 W is used to indicate the power transfer effect. The equivalent load resistance before the rectifier is calculated as 23.34 Ω using the following expression [33]:

$$R_{L\_\mathrm{eq}} = \frac{8}{\pi^2} \cdot R_{L\_\mathrm{actual}}. \tag{15}$$

Furthermore, the high voltage resonant nodes are connected to the aluminum frames to construct the capacitive coupling. The

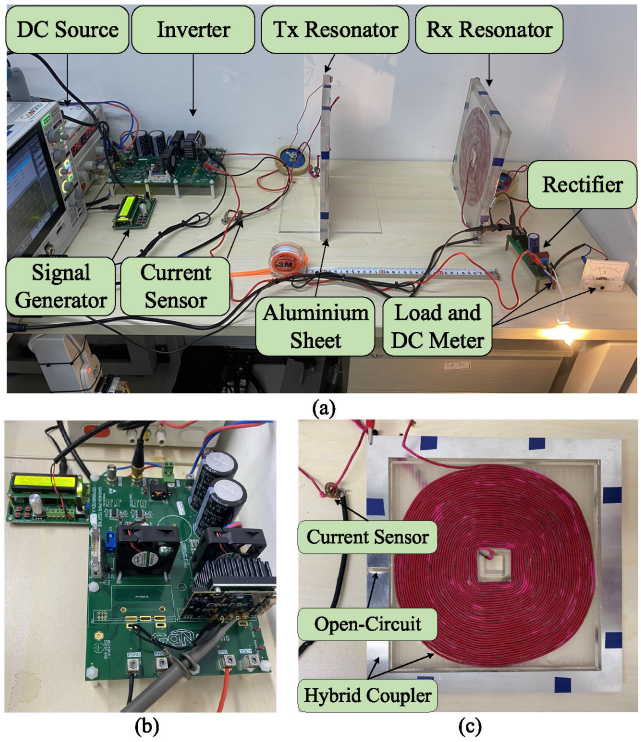

Fig. 15. Experimental setup. (a) Overview of experimental environment. (b) Inverter and signal generator. (c) Hybrid coupler and current sensor.

dimensions of the frames are in accordance with the simulation configurations. The practical parameters of the plates and the coils are listed in Table I. Particularly, an electrical wire is used to short-connect the low voltage nodes of the two sides. Moreover, the two metal frames are designed as open-circuit to reduce the eddy current along the borders, as seen in Fig. 15(c).

B. Experimental Results

First, the waveforms are recorded with a Tektronix MSO34 oscilloscope when the resonant frequency is fixed around 640 kHz with a lumped capacitor of 460 pF. During the experiments, the system is tuned to have a fixed load voltage. Then, the comparison of the proposed HWPT, the pure IPT, and the HWPT, but with a positive mutual inductance, is shown in Fig. 16, where the transfer gap is 30 cm. It can be observed that the Tx current of the HWPT is smaller than that of the pure IPT. This is because the HWPT has a larger reflected impedance. However, when Rx coil is flipped over, a larger Tx current will be needed, as seen in Fig. 16(c).

Then, the curves of the PTE versus the transfer gap are tested and compared. By integrating the product of the square voltage and sinusoidal current, the received and transmitted power can be calculated. Their ratios represent the ac-to-ac efficiencies. Then, the comparison of the tested efficiency values is shown in Fig. 17. On one hand, compared with the analytical results in Fig. 9, the tested ones are slightly lower. This is because the parasitic resistance of the capacitor is not considered, though,

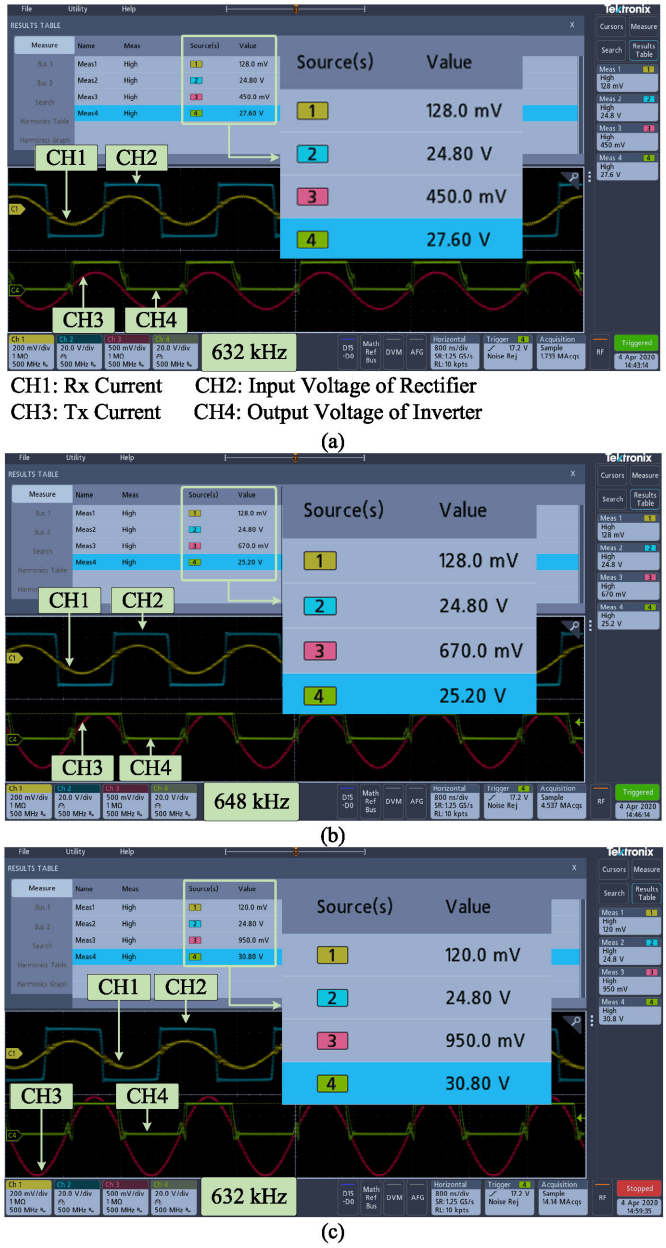

Fig. 16. Waveforms when the transfer gap is 30 cm and resonant frequency is around 640 kHz. (a) Proposed HWPT. (b) Pure IPT. (c) HWPT with a positive mutual inductance.

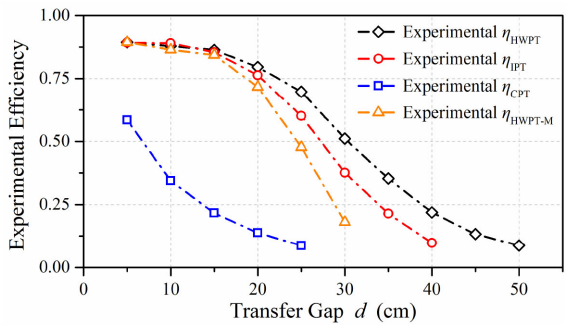

Fig. 17. Comparison of experimental efficiency values.

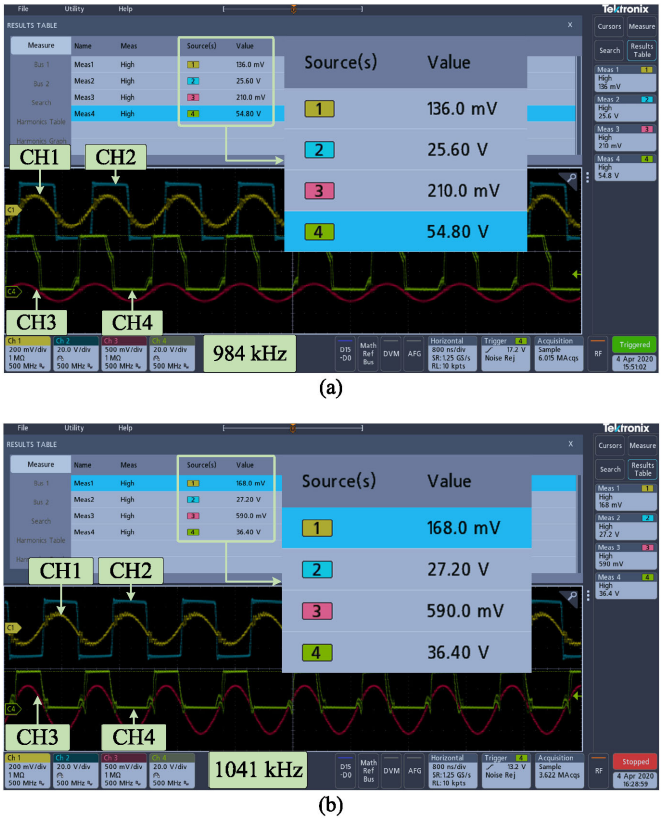

Fig. 18. Waveforms when transfer gap is 30 cm and resonant frequency is around 984 kHz. (a) Proposed HWPT. (b) Pure IPT.

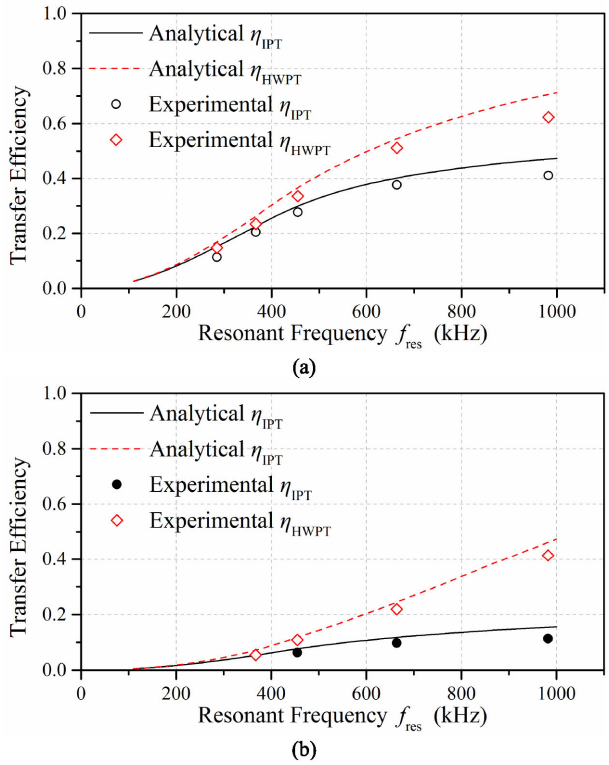

Fig. 19. Tested efficiency values with various resonant frequencies. (a) At 30-cm distance. (b) At 40-cm distance.

the general trend in Fig. 17 matches that in Fig. 9. On the other hand, compared with the pure IPT, the proposed HWPT exhibits an evident efficiency increment when the transfer gap is large. For instance, the efficiency increments at 30, 35, and 40 cm are 13.5%, 14%, and 12.1%, respectively. Particularly, when the transfer gap is larger than 40 cm, the efficiency of pure IPT is too low to be recorded, while that of HWPT still has a value of 13.3% at 45 cm. Moreover, the test results of $\eta_{\text{HWPT-M}}$ have verified that the two coupling coils should be wound in reverse directions. Otherwise, the added two metal frames will result in an efficiency decline. Additionally, the resonant frequency of the pure IPT is 648 kHz, while that of the HWPT is 632 kHz. This indicates that the stray capacitance of the metal frame has an influence on the overall compensation capacitance.

Next, the waveforms for 1-MHz resonant frequency are recorded. The original waveforms are given in Fig. 18. Compared with the waveforms in Fig. 16, the Tx current of the HWPT are further reduced. This indicates that a larger reflected impedance is generated with the resonant frequency increasing. Moreover, the Tx current ratio of the HWPT to the pure IPT in Fig. 18 is smaller than that in Fig. 16. This result shows that an increased resonant frequency will result in a larger contribution by the two extra coupling frames. The detailed testing conditions and results of Figs. 16 and 18 are summarized in Table IV in the Appendix.

After that, the curves of efficiency versus the resonant frequency are tested and compared. By changing the compensation capacitance, the resonant frequency is tuned to 285, 368, 455, 632, and 984 kHz in turn. Then, the frequency-dependent efficiencies are tested at 30 and 40 cm. The tested results are shown in Fig. 19. When resonant frequency is around 984 kHz, the tested values are about 5%−7% lower than the analytical ones. This is because the parasitic resistance of the 200-pF capacitor is relatively large. Even so, the general trend can still be concluded as: when the resonant frequency is relatively low, the HWPT has a close efficiency to that of pure IPT; when the resonant frequency is relatively high, the efficiency promotion will be more obvious. Thus, when transfer gap is large, the HWPT should work with a high resonant frequency to fully take advantage of the added coupling frames. Additionally, comparing Fig. 19(b) with Fig. 19(a), one can see that the efficiency promotion is more obvious when transfer gap is larger. This is because the coupling capacitance declines slower than the mutual inductance with the transfer gap increasing.

Finally, the LCC topology is verified for the proposed HWPT system. First, the implemented circuit is shown in Fig. 20(a). Here, the lumped compensation capacitance is 460 pF, and the nominal resonant frequency is 660 kHz. Considering that the practical resonant frequency of the HWPT is 632 kHz due to the stray capacitances, the values of L_{p1} and L_{p2} are both set to 6.3 μH. This value is slightly larger than the initially designed value of 5.8 μH. Then, the LCC topology's effectiveness against

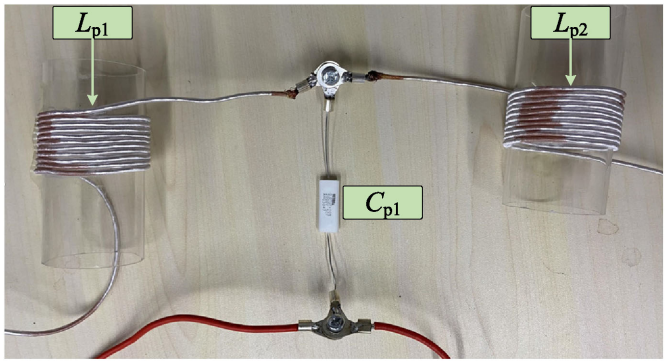

(a)

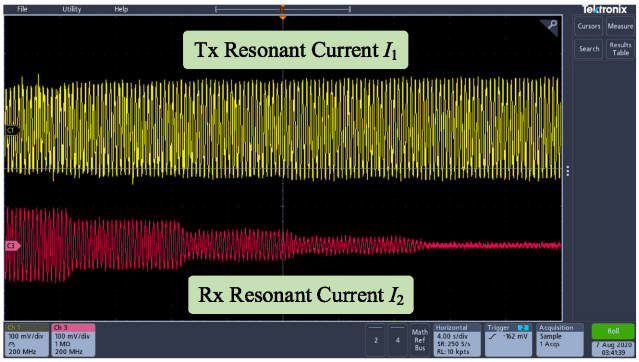

(b)

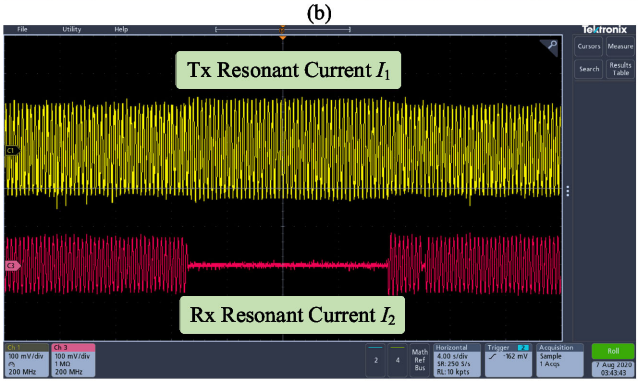

(c)

Fig. 20. LCC implementation and its effects. (a) Practical circuit implementation. (b) Effect against distance variation. (c) Effect against load variation.

the distance change is verified. As seen in Fig. 20(b), the receiver is gradually moved away from the transmitter. As a result, the Rx resonant current I_2 decreases gradually, while the Tx resonant current I_2 keeps almost constant. Furthermore, the effects against the load variation are verified. As seen in Fig. 20(c), the load is switched out and in, and I_1 stays at the same level. The results in Fig. 20(b) and (c) have indicated that the LCC topology is also effective for the proposed HWPT system to maintain a constant Tx resonant current against the distance and load variations.

V. Conclusion

In this article, a new compact HWPT system is proposed, which adopts a space-saving inner coil and outer frame structure as the hybrid coupler. The major contributions of the proposed system are summarized as follows.

1) The hybrid coupler for the inductive and capacitive combined coupling is greatly simplified. As a result, the proposed HWPT system becomes more flexible for practical implementation.
2) For the HWPT systems, an analysis in terms of reflected impedance is first conducted, which can clearly illustrate the mechanism of coupling and efficiency promotion.
3) The resonant frequency is optimized for various transfer gaps, which helps to instruct the practical system design.
4) The added two metal frames can effectively promote the coupling between the Tx and Rx sides. Thus, the coupling coil can be made smaller while maintaining the same transfer efficiency.
5) The proposed HWPT system presents an evident efficiency promotion at a large transfer gap. This feature makes it more suitable for large-gap WPT applications, such as for charging the PTLM devices.
6) Several practical concerns are considered, and the corresponding solutions are suggested. Particularly, a Tx side LCC topology is designed and verified against the distance and load variations.

However, due to the introduction of the extra capacitive route, the system becomes more complex in both the system model and the interference with the surroundings. In the future work, a practical HWPT application will be developed with a closed-loop control.

Appendix

TABLE III
Comparison of Surveyed HWPT Cases and This Article

Ref.	Number of Coupling Plates	Working Frequency	Efficiency	Size of Coupling Plates	Transfer Distance	Coupler Arrangement
[16]	4	1 MHz	90.8%	610*610 mm^2	150 mm	Increased horizontal area of one plate at each side
[17]	4	1 MHz	73.6%	450*450 mm^2	25 mm	Increased vertical size
[18]	4	800 kHz	91.9%	500*500 mm^2	150 mm	Increased horizontal area of two plates at each side
[19]	4	1 MHz	87.7%	600*600 mm^2	60 mm	Increased vertical size
[20]-[21]	4	6.78 MHz	80.0%	330*220 mm^2	0.05 mm	Increased horizontal area of two plates at each side
This paper	*2*	*Optimized for various transfer distance*	*86.4%*	*Square frame with 240-mm length and 20-mm width*	*150mm*	*One frame-shaped metal sheet*

TABLE IV
EXPERIMENTAL TESTING CONDITIONS AND RESULTS

Figure NO. [1*]	System Type	f_{res} (kHz)	V_{inv} (V) [2*]	I_1 (A) [3*]	V_{rec} (V)	I_2 (A)	P_{in} (V)	P_{out} (V)	η
Fig. 16(a)	HWPT	632	27.6	3.36	24.8	0.96	29.52	15.16	51.1%
Fig. 16 (b)	Pure IPT	648	25.2	5.0	24.8	0.96	40.11	15.16	37.6%
Fig. 16 (c)	HWPT-M [4*]	632	30.8	7.09	24.8	0.90	69.51	14.21	20.3%
Fig. 18 (a)	HWPT	984	54.8	1.57	25.6	1.01	27.39	16.46	60.5%
Fig. 18 (b)	Pure IPT	1041	36.4	4.40	27.2	1.25	50.98	21.64	42.5%

1* All these cases are tested with a 30-cm transfer gap.

2* V_{inv} represents the magnitude of the square-wave of the inverter's output; V_{rec} represents the magnitude of the square-wave of the rectifier's input.

3* For I_1 and I_2, the current sensors have a conversion ratio of 104 mV-1 A.

4* HWPT-M represents the HWPT system with a positive mutual inductance.

REFERENCES

[1] Q. Deng *et al.*, "Modeling and control of inductive power transfer system supplied by multiphase phase-controlled inverter," *IEEE Trans. Power Electron.*, vol. 34, no. 9, pp. 9303–9315, Dec. 2018.

[2] C. Jiang, K. T. Chau, C. Liu, and W. Han, "Design and analysis of wireless switched reluctance motor drives," *IEEE Trans. Ind. Electron.*, vol. 66, no. 1, pp. 245–254, Jan. 2019.

[3] H. Zhou, X. Gao, J. Lai, W. Hu, Q. Deng, and D. Zhou, "Natural frequency optimization of wireless power systems on power transmission lines," *IEEE Access*, vol. 6, pp. 14038–14047, Mar. 2018.

[4] C. Cai *et al.*., "Resonant wireless charging system design for 110 kV high voltage transmission line monitoring equipment," *IEEE Trans. Ind. Electron.*, vol. 66, no. 5, pp. 4118–4129, Feb. 2018.

[5] J. Dai and D. C. Ludois, "A survey of wireless power transfer and a critical comparison of inductive and capacitive coupling for small gap applications," *IEEE Trans. Power Electron.*, vol. 30, no. 11, pp. 6017–6029, Nov. 2015.

[6] Y. Xiao, C. Liu, Y. Huang, and S. Liu, "Concurrent wireless power transfer to multiple receivers with additional resonant frequencies and reduced power switches," *IEEE Trans. Ind. Electron.*, vol. 67, no. 11, pp. 9292–9301, Nov. 2020.

[7] C. Jiang, K. T. Chau, C. Liu, C. H. T. Lee, W. Han, and W. Liu, "Move-and-charge system for automatic guided vehicles," *IEEE Trans. Magn.*, vol. 54, no. 11, Nov. 2018, Art. no. 8600105.

[8] C. Jiang, K. T. Chau, C. Liu, and W. Han, "Design and analysis of wireless switched reluctance motor drives," *IEEE Trans. Ind. Electron.*, vol. 66, no. 1, pp. 245–254, Jan. 2019.

[9] Y. Huang, C. Liu, Y. Xiao, and S. Liu, "Separate power allocation and control method based on multiple power channels for wireless power transfer," *IEEE Trans. Power Electron.*, vol. 35, no. 9, pp. 9046–9056, Sep. 2020.

[10] M. P. Theodoridis, "Effective capacitive power transfer," *IEEE Trans. Power Electron.*, vol. 27, no. 12, pp. 4906–4913, Dec. 2012.

[11] L. Fei, Z. Hua, H. Hofman, and C. C. Mi, "A double-sided LCLC-compensated capacitive power transfer system for electric vehicle charging," *IEEE Trans. Power Electron.*, vol. 30, no. 11, pp. 6011–6014, Nov. 2015.

[12] S. Li, Z. Liu, H. Zhao, L. Zhu, C. Shuai, and Z. Chen, "Wireless power transfer by electric field resonance and its application in dynamic charging," *IEEE Trans. Power Electron.*, vol. 63, no. 10, pp. 6602–6612, Oct. 2016.

[13] R. Mai, B. Luo, Y. Chen, and Z. He, "Double-sided CL compensation topology-based component voltage stress optimization method for capacitive power transfer charging system," *IET Power Electron*., vol. 11, no. 7, pp. 1153–1160, Jun. 2018.

[14] H. Zhang, F. Lu, H. Hofmann, W. Liu, and C. C. Mi, "A four-plate compact capacitive coupler design and LCL-compensated topology for capacitive power transfer in electric vehicle charging application," *IEEE Trans. Power Electron.*, vol. 31, no. 12, pp. 8541–8551, Jan. 2016.

[15] D. Vincent, P. H. Sang, and S. S. Williamson, "Feasibility study of hybrid inductive and capacitive wireless power transfer for future transportation," in *Proc. IEEE Transp. Electrific. Conf. Expo (ITEC)*, 2017, pp. 229–233.

[16] F. Lu, H. Zhang, H. Hofmann, and C. C. Mi, "An inductive and capacitive combined wireless power transfer system with LC-compensated topology," *IEEE Trans. Power Electron.*, vol. 31, no. 12, pp. 8471–8482, Dec. 2016.

[17] F. Lu, H. Zhang, H. Hofmann, and C. C. Mi, "An inductive and capacitive integrated coupler and its LCL compensation circuit design for wireless power transfer," in *Proc. IEEE Energy Convers. Congr. Expo. (ECCE)*, 2016, pp. 1–5.

[18] B. Luo, T. Long, R. Mai, R. Dai, Z. He, and W. Li, "Analysis and design of hybrid inductive and capacitive wireless power transfer for high power applications," *IET Power Electron*., vol. 11, no. 14, pp. 2263–2270, Nov. 2018.

[19] B. Luo, T. Long, L. Guo, R. Dai, R. Mai, and Z. He, "Analysis and design of inductive and capacitive hybrid wireless power transfer for railway applications," *IEEE Trans. Ind. Appl.*, vol. 56, no. 3, pp. 3034–3042, May 2020.

[20] X. Chen, S. Yu, and X. Yang, "Hybrid wireless power transfer," in *Proc. Ind. Electron. Soc., IECON*, 2017, pp. 5348–5352.

[21] X. Chen, S. Yu, T. H. R. Li, and X. Yang, "An efficient hybrid wireless power transfer system with less gain fluctuation," in *Proc. IEEE Int. Power Electron. Appl. Conf. (PEAC)*, 2018, pp. 1–4.

[22] J. Shin *et al.*, "Design and implementation of shaped magnetic-resonance-based wireless power transfer system for roadway-powered moving electric vehicles," *IEEE Trans. Power Electron.*, vol. 61, no. 3, pp. 1179–1192, Mar. 2014.

[23] L. L. Grigsby, "Transmission line parameters," in *Electric Power Engineering Handbook*, Boca Raton, FL, USA: CRC Press, 2007, ch. 13, Part II.

[24] F. Lu, H. Zhang, and C. Mi, "A two-plate capacitive wireless power transfer system for electric vehicle charging applications," *IEEE Trans. Power Electron.*, vol. 33, no. 2, pp. 964–969, Feb. 2018.

[25] X. Gao, H. Zhou, W. Hu, Q. Deng, G. P. Liu, and J. Lai, "Capacitive power transfer through virtual self-capacitance route," *IET Power Electron*., vol. 11, no. 6, pp. 1110–1118, May 2018.

[26] T. M. Minteer, "The many capacitance terms of two parallel discs in free space," *Eur. J. Phys.*, vol. 35, no. 3, pp. 1–15, Apr. 2014.

[27] H. Nishiyama and M. Nakamura, "Capacitance of disk capacitors," *IEEE Trans. Compon. Hybrids Manuf. Technol.*, vol. 16, no. 3, pp. 360–366, May 1993.

[28] Y. P. Su, X. Liu, and S. Y. Ron Hui, "Mutual inductance calculation of movable planar coils on parallel surfaces," *IEEE Trans. Power Electron.*, vol. 24, no. 4, pp. 1115–1123, Apr. 2009.

[29] S. Cheon, Y. H. Kim, S. Y. Kang, M. L. Lee, J. M. Lee, and T. Zyung, "Circuit-model-based analysis of a wireless energy-transfer system via coupled magnetic resonances," *IEEE Trans. Ind. Electron.*, vol. 58, no. 7, pp. 2906–2914, Jul. 2014.

[30] J. Acero, C. Carretero, I. Lope, R. Alonso, O. Lucia, and J. M. Burdio, "Analysis of the mutual inductance of planar-lumped inductive power transfer systems," *IEEE Trans. Ind. Electron.*, vol. 60, no. 1, pp. 410–420, Jan. 2013.

[31] W. G. Hurley *et al.*, "A unified approach to the calculation of self-and mutual-inductance for coaxial coils in air," *IEEE Trans. Power Electron.*, vol. 30, no. 11, pp. 6155–6162, Nov. 2015.

[32] G. Wei, X. Jin, C. Wang, J. Feng, C. Zhu, and M. I. Matveevich, "An automatic coil design method with modified AC resistance evaluation for achieving maximum coil-coil efficiency in WPT systems," *IEEE Trans. Power Electron.*, vol. 35, no. 6, pp. 6114–6126, Jun. 2020.

[33] Q. Deng *et al.*, "Frequency-dependent resistance of Litz-wire square solenoid coils and quality factor optimization for wireless power transfer," *IEEE Trans. Ind. Electron.*, vol. 63, no. 5, pp. 2825–2837, May 2016.

[34] J. Liu, Q. Deng, D. Czarkowski, M. K. Kazimierczuk, H. Zhou, and W. Hu, "Frequency optimization for inductive power transfer based on AC resistance evaluation in Litz-wire coil," *IEEE Trans. Power Electron.*, vol. 34, no. 3, pp. 2355–2363, Mar. 2019.
[35] Q. Zhu, L. Wang, Y. Guo, C. Liao, and F. Li, "Applying LCC compensation network to dynamic wireless EV charging system," *IEEE Trans. Ind. Electron.*, vol. 63, no. 10, pp. 6557–6567, Oct. 2016.
[36] S. Li, W. Li, J. Deng, T. D. Nguyen, and C. C. Mi, "A double-sided LCC compensation network and its tuning method for wireless power transfer," *IEEE Trans. Veh. Technol.*, vol. 64, no. 6, pp. 2261–2273, Jun. 2015.
[37] S. Y. Choi, S. Y. Jeong, B. W. Gu, G. C. Lim, and C. T. Rim, "Ultraslim S-type power supply rails for roadway-powered electric vehicles," *IEEE Trans. Power Electron.*, vol. 30, no. 11, pp. 6456–6468, Nov. 2015.
[38] N. Hatchavanich, M. Konghirun, and A. Saengswang, "The analysis of series-parallel-parallel compensation current source inverter for wireless power transfer in EVs charging application," in *Proc. IEEE 12th Int. Conf. Power Electron. Drive Syst. (PEDS)*, pp. 1093–1097, Dec. 2017.
[39] M. Fu, H. Yin, X. Zhu, and C. Ma, "Analysis and tracking of optimal load in wireless power transfer systems," *IEEE Trans. Power Electron.*, vol. 30, no. 7, pp. 3952–3963, Jul. 2015.

Xingran Gao received the B.S. degree in automation and the Ph.D. degree in mechatronics from Wuhan University, Wuhan, China, in 2013 and 2019, respectively.

He is currently working as a Postdoctor in electrical and electronic engineering with the City University of Hong Kong, Hong Kong. His main research interests include the power electronics, wireless power transmission, electric vehicle technology, and motor drive technologies.

Chunhua Liu (Senior Member, IEEE) received the B.Eng. and M.Eng. degrees in automatic control from Beijing Institute of Technology, Beijing, China, in 2002 and 2005, respectively, and the Ph.D. degree in electrical and electronic engineering from The University of Hong Kong, Hong Kong, in 2009.

Currently, he serves as an Associate Professor with the School of Energy and Environment, City University of Hong Kong, Hong Kong. His research interests include electric machines and drives, electric vehicles and aircrafts, electric robotics and ships, renewables and microgrid, power electronics, and wireless power transfer. In these areas, he has authored or coauthored over 200 refereed papers.

Dr. Liu is currently an Associate Editor for IEEE TRANSACTION ON INDUSTRIAL ELECTRONICS and Editor for IEEE TRANSACTIONS ON VEHICULAR TECHNOLOGY and IEEE TRANSACTIONS ON ENERGY CONVERSION. Also, he is an Editor for *Energies*, Subject Editor for *IET Renewable Power Generation*, Subject Editor for *Wireless Power Transfer* (Cambridge University), Associate Editor for *Open Journal of the Industrial Electronics Society*, Associate Editor for *IEEE Chinese Journal of Electrical Engineering*, and Editor for IEEE TRANSACTIONS ON MAGNETICS—Conference. In addition, he is Chair and Founder of Hong Kong Chapter, IEEE Vehicular Technology Society.

Hong Zhou (Member, IEEE) received the B.S. degree in industrial automation from the Central South University of Technology, Changsha, China, in 1982, the M.Sc. degree in industrial automation from Chongqing University, Chongqing, China, in 1988, and the Ph.D. degree in mechanical engineering from Wuhan University, Wuhan, China, in 2006.

He has been a Professor with Department of Automation (now the Department of Artificial Intelligence and Automation), Wuhan University, since 2000. His research interests include wireless power transfer, smart grid, and networked control systems.

Wenshan Hu (Member, IEEE) received the B.S. and M.Sc. degrees in control theory and applications from Wuhan University, Wuhan, China, in 2002 and 2004, respectively, and the Ph.D. degree in control engineering from the University of Glamorgan, Pontypridd, U.K., in 2008.

He is currently a Professor with the Department of Artificial Intelligence and Automation, Wuhan University. His research interests include network-based control laboratories and wireless power transfer.

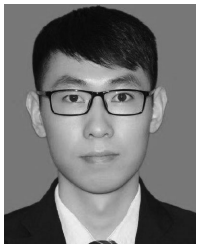

Yongcan Huang (Student Member, IEEE) received the B.Eng. and M.Eng. degrees in control science and engineering from Chongqing University, Chongqing, China, in 2015 and 2018, respectively. He is currently working toward the Ph.D. degree in electrical and electronic engineering with the City University of Hong Kong, Hong Kong.

His main research interests include the power electronics, wireless power transmission, electric vehicle technology, and control of multiphase drive systems.

Yang Xiao (Student Member, IEEE) received the B.Eng. degree in electrical engineering and automation from Soochow University, Suzhou, China, in 2014, and the M.Eng. degree in electrical engineering from Southeast University, Nanjing, China, in 2017. He is currently working toward the Ph.D. degree with the City University of Hong Kong, Hong Kong.

His main research interests include wireless power transmission, electric vehicle battery chargers, and control of multiphase drive systems.

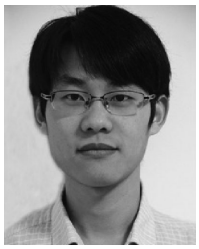

Zhongcheng Lei (Member, IEEE) received the B.S. degree in automation and the Ph.D. degree in mechatronic engineering from Wuhan University, Wuhan, China, in 2014 and 2019, respectively.

He is currently a Postdoctoral Fellow with the School of Electrical Engineering and Automation, Wuhan University. His research interests include networked control systems and web-based remote and virtual laboratories.

Jing Chen received the B.S. degree in mechanical engineering in 2016 from the Wuhan University, Wuhan, China, where he is currently working toward the Ph.D. degree with the School of Electrical Engineering and Automation.

His current research interests include the high-power inverter technology, topology design and optimization of wireless power transfer, and hybrid energy supply technology.